Defect-Engineering by Solvent Mediated Mild Oxidation as a Tool to Induce Exchange Bias in Metal Doped Ferrites

Beatrice Muzzi, Martin Albino, Michele Petrecca, Claudia Innocenti, César de Julián Fernández, Giovanni Bertoni, M. Ricardo Ibarra, Mogens Christensen, Maxim Avdeev, Clara Marquina,* and Claudio Sangregorio*

The crystal site occupancy of different divalent ions and the induction of lattice defects represent an additional tool for modifying the intrinsic magnetic properties of spinel ferrites nanoparticles. Here, the relevance of the lattice defects is demonstrated in the appearance of exchange-bias and in the improvement of the magnetic properties of doped ferrites of 20 nm, obtained from the mild oxidation of core@shell (wüstite@ferrite) nanoparticles. Three types of nanoparticles ($Fe_{0.95}O@Fe_3O_4$, $Co_{0.3}Fe_{0.7}O@Co_{0.8}Fe_{2.2}O_4$ and $Ni_{0.17}Co_{0.21}Fe_{0.62}O@Ni_{0.4}Co_{0.3}Fe_{2.3}O_4$) are oxidized. As a result, the core@shell morphology is removed and transformed in a spinel-like nanoparticle, through a topotactic transformation. This study shows that most of the induced defects in these nanoparticles and their magnetic properties are driven by the inability of the $Co^{(II)}$ ions at the octahedral sites to migrate to tetrahedral sites, at the chosen mild oxidation temperature. In addition, the appearance of crystal defects and antiphase boundaries improves the magnetic properties of the starting compounds and leads to the appearance of exchange bias at room temperature. These results highlight the validity of the proposed method to impose novel magnetic characteristics in the technologically relevant class of nanomaterials such as spinel ferrites, expanding their potential exploitation in several application fields.

1. Introduction

In the last decades, the emergence of new-generation technologies have pushed the research activity toward the development of nanomaterials. Nanosized materials reveal excellent and unique optical, electrical, catalytic, medical, biological and magnetic properties,[1–6] which arise from the fine tuning of the nanostructure characteristics (e.g. size, shape, or a combination of different nano-sized materials). Among others, magnetic nanoparticles (NPs) can be exploited in several applications such as biomedicine,[7,8] catalysis,[9,10] magnetic recording,[11] and as permanent magnets.[12,13] In particular, thanks to the large variety of physical properties (high magnetic permeability, high magnetic anisotropy or high electrical resistance), spinel ferrite-based nanostructures, either as single phase or enclosed in complex architectures, have

B. Muzzi
Department of Biotechnology
Chemistry and Pharmacy
University of Siena
Siena I-53100, Italy

B. Muzzi, C. Innocenti, C. Sangregorio
Istituto di Chimica dei Composti Organometallici (ICCOM)
Consiglio Nazionale delle Ricerche (CNR)
Sesto Fiorentino (FI) I-50019, Italy
E-mail: csangregorio@iccom.cnr.it

B. Muzzi, M. Albino, M. Petrecca, C. Innocenti, C. Sangregorio
Department of Chemistry "U. Schiff"
University of Florence and INSTM
Sesto Fiorentino, (FI) I-50019, Italy

C. de Julián Fernández
Istituto dei Materiali per l' Elettronica ed il Magnetismo (IMEM)
Consiglio Nazionale delle Ricerche (CNR)
Parma I-43124, Italy

G. Bertoni
CNR – Istituto Nanoscienze
Modena I-41125, Italy

M. R. Ibarra, C. Marquina
Instituto de Nanociencia y Materiales de Aragón (INMA)
Consejo Superior de Investigaciones Científicas (CSIC)-Universidad de Zaragoza
Zaragoza 50009, Spain
E-mail: clara@unizar.es

M. R. Ibarra, C. Marquina
Departamento de Física de la Materia Condensada
Universidad de Zaragoza
Zaragoza 50009, Spain

M. R. Ibarra
Laboratorio de Microscopias Avanzadas (LMA)
Universidad de Zaragoza
Zaragoza 50009, Spain

been extensively investigated for these applications.[14,15] Recent studies on iron-based NPs (e.g. Fe_3O_4, core@shell $Fe_{1-X}O@Fe_3O_4$, etc.), revealed that defect-engineering at the nanoscale can be a novel approach to tailor the magnetic properties of NPs (e.g. high coercive field, exchange bias)[16] Indeed, there is a close correlation between the magnetic properties and the crystal structure (e.g. lattice defects, ions distribution). Lappas et. al.[17] found by Monte Carlo simulations that the magnetic anisotropy energy barrier of defected iron-oxides NPs can be tuned as a function of the lattice defect (vacancies, dislocations, stacking faults and antiphase boundaries) and the uncompensated spins in the defected regions can induce some magnetic phenomena, such as the exchange bias (EB).[18–20] This latter is commonly observed in exchange coupled antiferromagnetic (AFM)/ferr(i)magnetic F(i)M nano-heterostructures, including core@shell (CS) NPs, when the system is cooled from room temperature through the ordering temperature of the AFM component in the presence of an external magnetic field. Although the exact nature and the phenomenology of the EB are still under debate, it is generally accepted that it originates from the pinning force asserted by the AFM phase on the magnetic moment of the F(i)M interface uncompensated spins. The latter will thus require a higher external magnetic field, for reversing the magnetization toward the direction opposite to the cooling field.[12,20–25] As a result, a horizontal shift (EB field, H_E) of the hysteresis loops, and the increase of the coercive field (H_C) are observed.

The controlled oxidation of CS AFM@F(i)M $Fe_{1-x}O@Fe_3O_4$ NPs has proven to be an efficient strategy to introduce defects into the ferrite spinel lattice. Wetterskog et al.[26] observed that under controlled oxidation, the lattice strain at the CS interface was released as the $Fe_{1-x}O$ core oxidized, but some defects in the crystal structure, such as antiphase boundaries (APBs)[27] were still retained in the final single phase Fe_3O_4. Indeed, the wüstite structure is characterized by octahedral (*Oh*) sites, occupied by $Fe^{(II)}$ only, which, after oxidation, evolves into a cubic spinel structure. In the latter, both $Fe^{(II)}$ and $Fe^{(III)}$ are present and they coordinate with oxygen differently: $Fe^{(II)}$ cations coordinate with *Oh* symmetry (as in wustite), whereas $Fe^{(III)}$ cations coordinate equally with both *Oh* and tetrahedral (*Td*) symmetry. Therefore, the *Td* sites in the spinel originate new crystal planes, that are not present in the wüstite phase, which causes the oxidation-generated defects to persist, even when oxidation to single-phase ferrite is complete.[17,26,28–36]

This approach was successfully applied by some of us to the synthesis of 10 nm defected cobalt ferrite NPs, which thanks

to the large contribution to the magneto-crystalline anisotropy from $Co^{(II)}$ ions, in addition to the oxidation-generated defects, exhibited very large EB.[27] However, their magnetic behavior was strongly affected by the contribution of the AFM component. This feature was ascribed to the formation of a large magnetic disorder spinel ferrite domains.[37] A possible strategy to overcome the drawback is to add to the defected cobalt ferrite a second divalent cation able to restore the magnetic order while retaining the lattice defects. Recently, Muzzi et al. demonstrate that the introduction of $Ni^{(II)}$ in the crystal lattice of CS $Ni_{0.17}Co_{0.21}Fe_{0.62}O@Ni_{0.4}Co_{0.3}Fe_{2.3}O_4$, allowed for partially recovering the magnetic order in the ferrite shell, leading to a more pronounced F(i)M character in the ferrites moiety.

Starting from these considerations, we here present an investigation aimed to rationalize the effect of $Co^{(II)}$ and $Ni^{(II)}$ on the lattice defects induced in spinel ferrite NPs by solvent-mediated mild oxidation of AFM@FiM precursors, and on how they affect the magnetic properties. With this aim, 20 nm CS $Fe_{0.95}O@Fe_3O_4$, $Co_{0.3}Fe_{0.7}O@Co_{0.8}Fe_{2.2}O_4$ and $Ni_{0.17}Co_{0.21}Fe_{0.62}O@Ni_{0.4}Co_{0.3}Fe_{2.3}O_4$ NPs synthesized by thermal decomposition method,[37] were oxidized to the single phase $Fe_{3-x}O_4$ (FeO-oxy), $Co_yFe_{3-y}O_4$ (CoFeO-oxy), and $Ni_zCo_yFe_{3-y-z}O_4$ (NiCoFeO-oxy) nanocrystals. The different site occupancy and the formation of the lattice defects in the fully oxidized nickel-cobalt and cobalt-substituted ferrites lead to the appearance of EB, increasing the coercive field value and consequently, the energy that can be stored in the materials.[37] Importantly, this peculiar variation is inherent to the transformation that occurs during the oxidation process, since the same behavior is not observed when the same doped-ferrite nanoparticles are synthesized by one-pot thermal decomposition,[38,39] sol–gel method[40] or in single-crystal thin films.[41–43] The peculiar magnetic behavior observed in the $Co_yFe_{3-y}O_4$ and $Ni_zCo_yFe_{3-y-z}O_4$ NPs confirmed that the combination of lattice defects, induced by solvent-mediated oxidation, and divalent metal ion doping is a promising method to impose novel magnetic properties to nanostructured materials, as a matter of fact generating a novel class of nanomaterials.

2. Results and Discussion

The mild oxidation of the CS $Fe_{0.95}O@Fe_3O_4$, $Co_{0.3}Fe_{0.7}O@Co_{0.8}Fe_{2.2}O_4$, and $Ni_{0.17}Co_{0.21}Fe_{0.62}O@Ni_{0.4}Co_{0.3}Fe_{2.3}O_4$ NPs[37] in a high boiling temperature solvent (310 °C) led to nanocrystals of 20 ± 3 nm for FeO-oxy, **Figure 1**a, and NiCoFeO-oxy, Figure 1c, and 22 ± 4 nm for CoFeO-oxy, Figure 1b, with truncated octahedron shape ascribed to (111) faces well-formed and sharp. The size and size distribution remained almost unaltered after the thermal annealing (Figures S1 and S2, Supporting Information) confirming the validity of the approach used for the oxidation step to avoid particle aggregation. For the whole series, the NPs were capped by an oleate surfactant layer, estimated by CHN analysis as ca. 25% w/w.

In **Figure 2** (left panel) scanning transmission electron microscopy-electron energy loss spectroscopy (STEM-EELS) chemical composition mapping, after Principal Component Analysis (PCA) decomposition, for a single NP of FeO-oxy, CoFeO-oxy, and NiCoFeO-oxy, respectively, is shown with the corresponding element distribution. The distribution of cobalt and nickel in these NPs remained homogeneous after the

M. Christensen
Department of Chemistry and iNANO
Aarhus University
Langelandsgade 140, Aarhus C DK-8000, Denmark

M. Avdeev
Australian Nuclear Science and Technology Organisation (ANSTO)
New Illawarra Road, Lucas Heights, NSW 2234, Australia

M. Avdeev
School of Chemistry
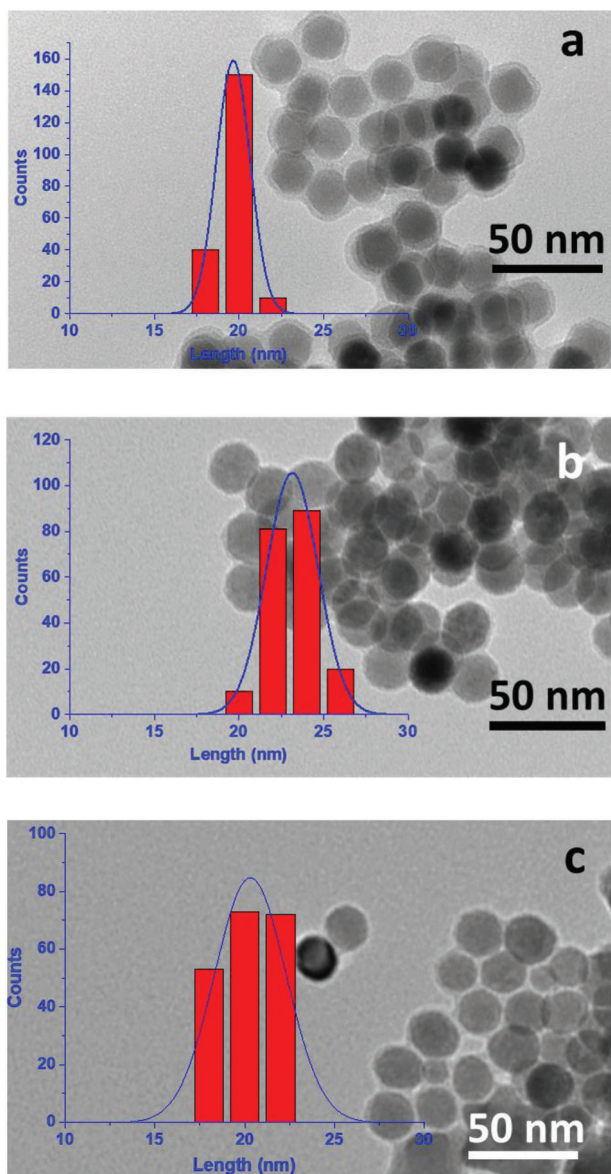The University of Sydney
Sydney, NSW 2006, Australia

**ADVANCED
SCIENCE NEWS**

www.advancedsciencenews.com

**small
methods**

www.small-methods.com

Figure 1. Transmission electron microscopy (TEM) images of a) FeO-oxy, b) CoFeO-oxy, and c) NiCoFeO-oxy NPs and the corresponding size distributions.

oxidation process, underlining the suitability of the chosen method (Figure S3, Supporting Information). The chemical quantification analysis performed on normalized EELS spectra (Figure 2, right panel) indicated the final stoichiometric compositions: Fe_3O_4 for FeO-oxy, $CoFe_2O_4$ for CoFeO-oxy, and $Ni_{0.4}Co_{0.6}Fe_2O_4$ for NiCoFeO-oxy, were attained. The formation of the Fe_3O_4 phase was further confirmed by the magnetization vs temperature curve that displayed the characteristic feature of the Verwey transition at ca. 100 K (Figure S5, Supporting Information).

The crystal structure evolution was investigated by acquiring Ultra-High Resolution Transmission Electron Microscope (UHRTEM) images of the NPs before and after oxidation and analyzing their local Fast Fourier Transformation (FFT). In

Figure 3 (left panel), the UHRTEM image of a NiCoFeO NP (i.e. $Ni_{0.17}Co_{0.21}Fe_{0.62}O@Ni_{0.4}Co_{0.3}Fe_{2.3}O_4$ before oxidation) is shown as a representative, while images of FeO ($Fe_{0.95}O@Fe_3O_4$) and CoFeO ($Co_{0.3}Fe_{0.7}O@Co_{0.8}Fe_{2.2}O_4$) NPs are reported in the Figures S1 and S2 (Supporting Information). The CS morphology can be clearly distinguished in Figure 3, left. The FFT analysis, performed on the two red squares areas, *a* (core) and *b* (shell), revealed, respectively, the rock-salt (RS, $Fm\bar{3}m$) structure of the $Ni_{0.17}Co_{0.21}Fe_{0.62}O$ core, and reflections corresponding to the cubic spinel structure (S, $Fd\bar{3}m$) of the $Ni_{0.4}Co_{0.3}Fe_{2.3}O_4$ shell (Figure 3a',b').[37] After the oxidation step at 310 °C, only one phase can be distinguished by the UHRTEM analysis (Figure 3, right panel). FFT analysis on the red square *c* area (Figure 3c') indeed, revealed reflections related only to the S structure in the whole NP. The annealing-oxidation treatment here proposed, induces the complete transformation of the metal monoxide core into the spinel phase, removing the CS architecture.

Although UHRTEM suggests the NPs have a high degree of crystalline order, Bragg filtering was applied to investigate the presence of crystal defects. The $(440)_S$ Bragg filtering images (**Figure 4**) obtained from the FFT of the FeO-oxy, CoFeO-oxy, and NiCoFeO-oxy UHRTEM images, show a continuous non-defective S phase for the FeO-oxy NP, while images of the doped ferrites depict a defective structure with a considerable number of APB. This evolution toward a nonhomogeneous crystal structure can be attributed to the presence of the $Co^{(II)}$ in the lattice.[27] On the other hand, also $Ni^{(II)}$ in NiCoFeO-oxy, which coordinates only in *Oh* symmetry,[44] may hinder the formation of the S cubic structure.

In **Figure 5**, the powder X-Ray diffraction (PXRD) patterns of samples before and after mild oxidation are shown. For the pre-oxidized samples, the monoxide structure (black pattern), corresponding to the $Fm\bar{3}m$ space group, was observed. The peak (311) at $2\theta = 36.5$ degrees, related to the cubic S structure $Fd\bar{3}m$, can be distinguished only for the FeO sample, suggesting the ferrite shell surrounding the monoxide core is thicker in these NPs, while it is too thin to give an appreciable signal for the cobalt and nickel-doped analogs.[37] After the oxidation, all the reflections observed in the PXRD pattern of FeO-oxy (red pattern) match for position and intensity those of the Fe_3O_4 reference pattern and the peak profile suggests a good crystallinity without defects. Conversely, the oxidative treatment carried out on the cobalt and the nickel-cobalt substituted samples led to some peculiarities: despite the position of all the peaks corresponding to those expected for an S structure, the profile and the relative intensities of some peaks present some differences. The three peaks at $2\theta = 37.0°$, $43.0°$, and $62.5°$, indexed as the $(222)_S$, $(400)_S$, and $(440)_S$ reflections of the doped spinel ferrite, respectively, are sharp, while the other four peaks, $(220)_S$, $(311)_S$, $(422)_S$, and $(511)_S$, are much broader. This feature can be explained by considering that the two crystallographic structures, RS and S, share a very similar cubic packing of oxygen anions. Indeed, the $(222)_S$, $(400)_S$, and $(440)_S$ reflections of the S structure correspond to the same families of planes $(111)_{RS}$, $(200)_{RS}$, and $(220)_{RS}$ of the monoxide structure. In particular, the progressive growth of the oxidized phase occurs by the displacement of the RS/S interface along $(111)_{RS}//(222)_S$, $(200)_{RS}//(400)_S$, and $(220)_{RS}//(440)_S$ planes. $Fe^{(II)}$ in the monoxide and part of the $Fe^{(II)}/Fe^{(III)}$ in the S occupy the *Oh* positions, corresponding to

**ADVANCED
SCIENCE NEWS**

www.advancedsciencenews.com
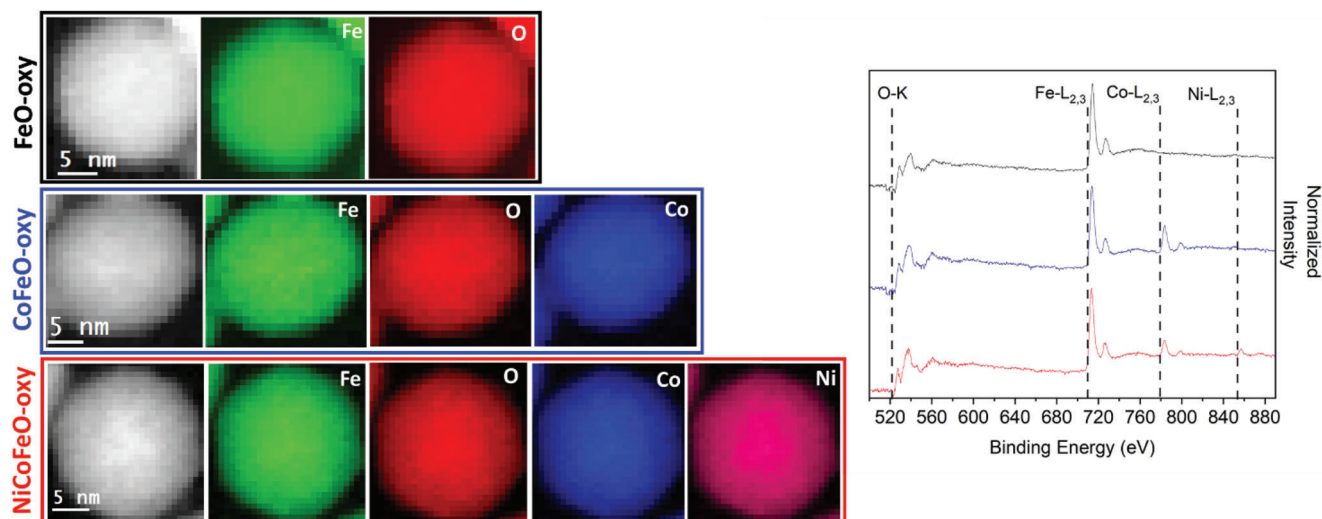
**small
methods**

www.small-methods.com

Figure 2. Left: mapping and distributions of oxygen (O-K edge, red), iron (Fe-L$_{2,3}$ edge, green), cobalt (Co-L$_{2,3}$ edge, blue) and nickel (Ni-L$_{2,3}$ edge, magenta) inside one NP of FeO-oxy (black rectangle, top), CoFeO-oxy (blue rectangle, middle), NiCoFeO-oxy (red rectangle, bottom). The colour intensity is proportional to the relative concentration of the corresponding ion. Right: EELS spectra of FeO-oxy (black line), CoFeO-oxy (blue line) and NiCoFeO-oxy (red line). The same analysis was performed on 10 NPs of each sample, providing the same results.

the $(200)_{RS}//(400)_S$ and $(220)_{RS}//(440)_S$ planes. Instead, the formation of the long-range ordered tetrahedral (*Td*) Fe$^{(III)}$ sublattice generates the $(220)_S$ planes in the S ferrite, which do not have a counterpart in the monoxide, potentially leading to a final defective iron spinel ferrite.[17,34] In fact, along the directions shared by the RS and S structures, the transformation from RS to S requires only a small rearrangement of the oxygen lattice, which can be easily achieved even at low annealing temperature, such as the one adopted in this work. Conversely, the rearrangement along the crystallographic directions not shared by the two cubic phases requires higher energy.

Interestingly, this peculiar behavior was observed only for the cobalt and nickel-doped-iron oxide nanocrystals. In fact, the evaluation of the microstrain by a Rietveld refinement of the PXRD

patterns, shows that for CoFeO-oxy and NiCoFeO-oxy the values derived from the broad peaks are three orders of magnitude higher than those derived from the sharp ones, while no difference is observed for FeO-oxy. Therefore, it can be argued that Fe$^{(II)}$ replacement in the pristine monoxide NPs plays a crucial role in the formation of a defective lattice during the structural transformation, with a consequent increase of the crystal lattice strain.

The strain maps obtained by Geometric Phases Analysis (GPA) measurements calculated for the crystallographic planes $(311)_S$ and $(440)_S/(220)_{RS}$ allowed us to estimate how much they are tilted from a reference position along the *x*- and *y*-axes (**Figure 6**). The red-green regions are related to the zero-strain value, while the yellow or blue-black areas correspond to the regions where the planes are strongly tilted (up to ± 35%).

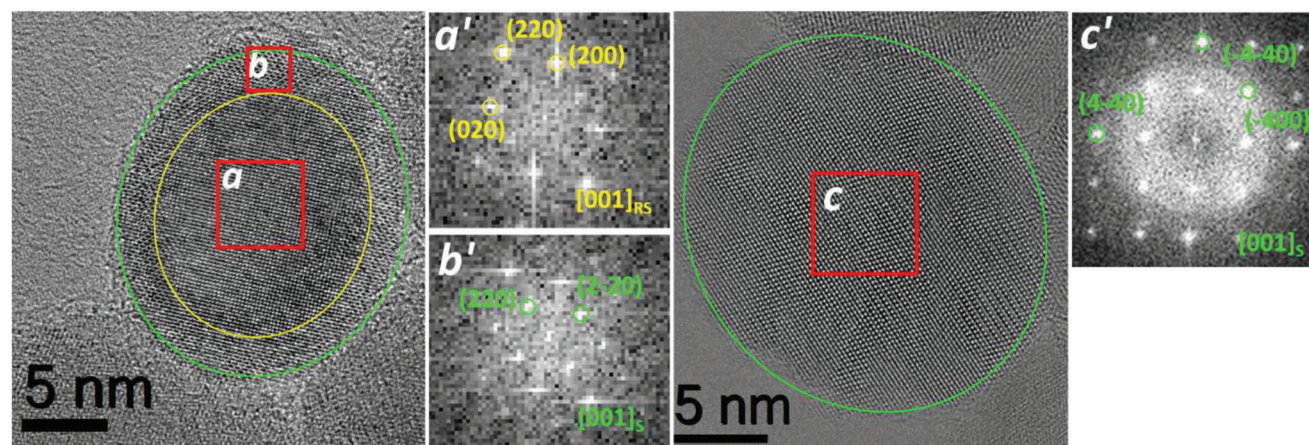**Figure 3.** Left: UHRTEM image of a NiCoFeO NP with the CS structure: the two red squares indicates the regions selected to identify the core (*a*) and the 2 nm thick shell (*b*); FFT analysis of the selected regions: the labelled spots are related to the crystallographic planes indexed as (*a'*) RS phase (*Fm$\bar{3}$m*), in zone axis [001]$_{RS}$ and (*b'*) S structure (*Fd$\bar{3}$m*), [001]$_S$. Right: UHRTEM image of a NiCoFeO-oxy NP: the core@shell structure disappeared and the FFT analysis of region *c* revealed the cubic spinel structure (*Fd$\bar{3}$m*), in zone axis [001]$_S$.

ADVANCED
SCIENCE NEWS

www.advancedsciencenews.com
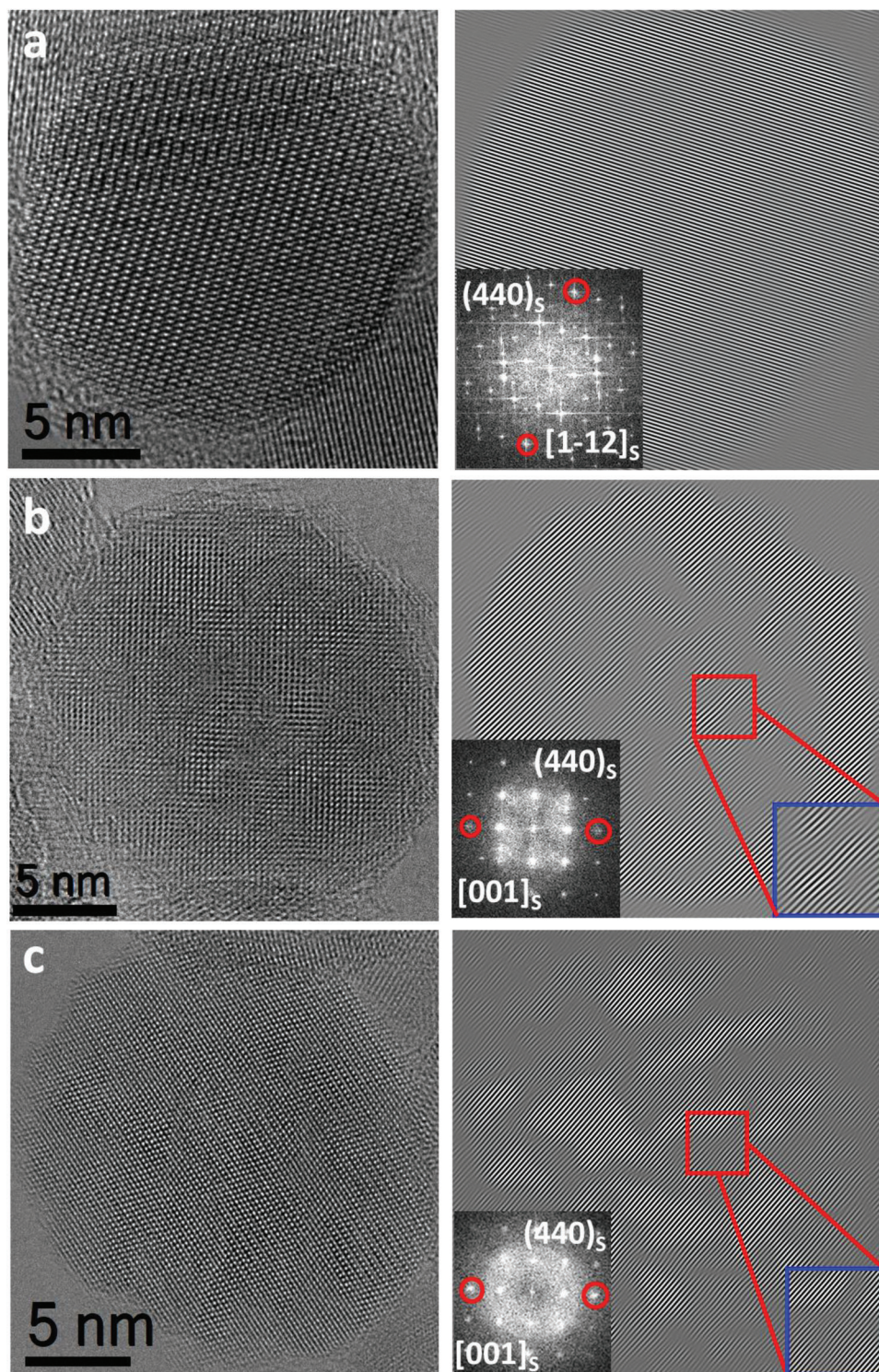
small
methods

www.small-methods.com

Figure 4. UHRTEM images of a FeO-oxy (a), CoFeO-oxy (b) and NiCoFeO-oxy (c) NPs oriented in zone axis $[001]_S$ and their corresponding Bragg filtered maps for the $(440)_S$ diffraction spots. The blue squares are enlargements of the selected area (red square) to highlight dislocation defects (e.g. APB) in $(440)s$ maps.
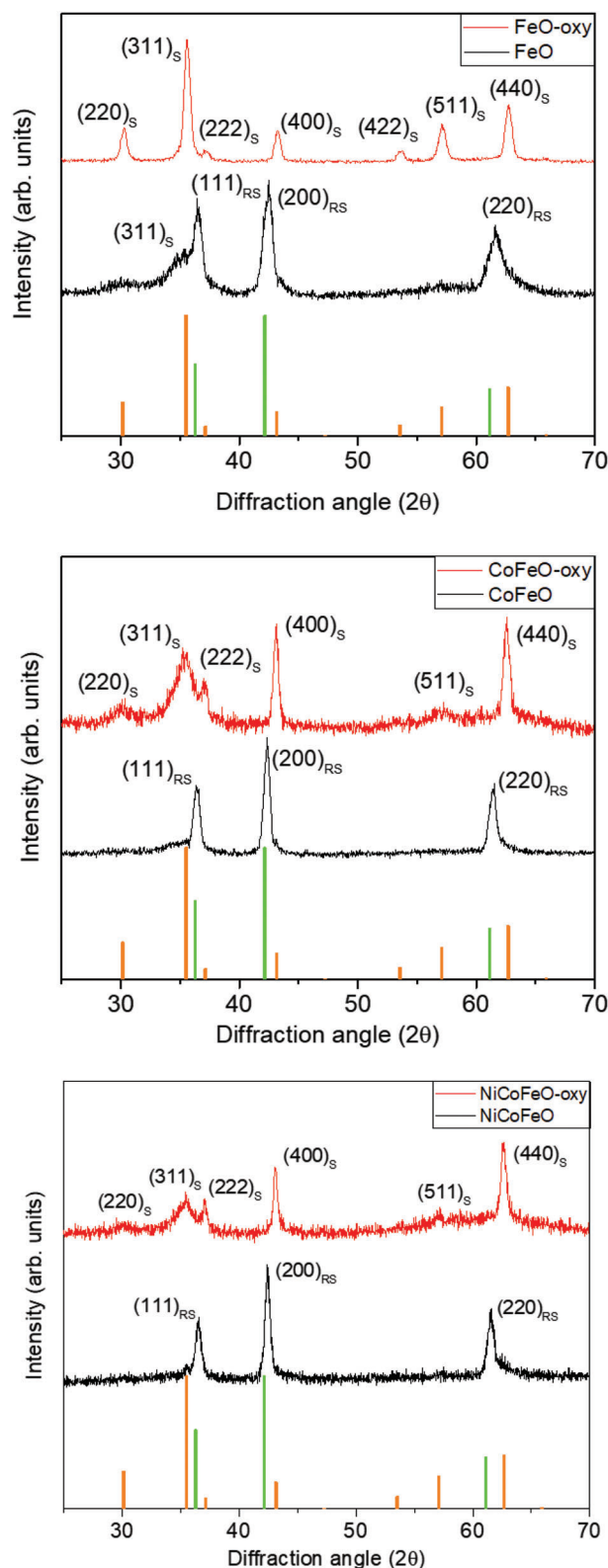
Figure 5. PXRD patterns of the three samples before (black pattern) and after (red pattern) solvent mediated oxidation treatment at 310°C; orange and green bars correspond to the reference pattern for Fe_3O_4 (JCPDS PDF #19-0629) and FeO (JCPDS PDF #73-2144), respectively. All the PXRD patterns are recorded using a Cu Kα (1.5406 Å) radiation source.

The strain mapping confirmed that the structural rearrangement along one of the new directions not shared by the two structures, $(311)_S$, results in a lattice strain higher than that observed when the atoms rearrange along a direction common to the two structures, $(440)_S/(220)_{RS}$.[45] In particular, this difference is more evident for CoFeO-oxy, and to a lower extent for NiCoFeO-oxy.

From the structural characterization by PXRD, Bragg filtered images, and lattice deformation profile it can be concluded that in the doped ferrite NPs the topotaxial oxidative growth of the S phase led to the formation of small spinel subdomain (mosaic texture) in a well-defined RS structure, underlining the key role of the Co(II) and Ni(II) in the crystal structure evolution. Previous studies on doped ferrites have shown that Co and Ni occupy different positions in the spinel structure. In $CoFe_2O_4$ NPs synthesized by thermal decomposition or by annealing, Co(II) is distributed between *Oh* and *Td* sites with inversion degrees in the 0.6-0.8 range.[13,44,46] Conversely, in $Ni_xFe_{3-x}O_4$ NPs ($x = 0.04$, 0.06 and 0.11), Ni(II) substitutes the Fe(II) in the *Oh* sites, independently of the stoichiometry.[44,47] To assess the Co(II) distribution, neutron powder diffraction was performed. Experiments were limited to CoFeO-oxy for which the different scattering lengths of Fe and Co (b(Fe) = 9.45 fm and b(Co) = 2.49 fm) ensures a good elemental contrast. Conversely, since b(Ni) = 10.3 fm is relatively close to the scattering length of Fe, NiCoFeO-oxy was not investigated. Therefore, in the following, it will be assumed all Ni(II) ions are coordinated with *Oh* symmetry. In **Figure 7** is reported the neutron powder diffraction pattern and, as a reference, the CoKα X-ray pattern recorded with a high-intensity source. The combined Rietveld refinement of the two patterns (see Supporting Information for details) displayed that Co(II) ions occupy only *Oh* sites. Moreover, the fitting shows ca. 15% of *Td*-vacancies, underlining a defective structure occurs in the *Td* sites lattice, which can be correlated to the presence of stacking fault, APB, and lattice microstrain in the final spinel.[17,26] This observation is in good agreement with the lattice deformation profile corresponding to the $(311)_S$ direction, which passes through the *Td* sites, reported in Figure 6. On the contrary, no strain is observed along directions corresponding to *Oh* sites, in good accordance with the lattice deformation profile corresponding to the $(440)_S/(220)_{RS}$ directions. Interestingly, when CoFeO-oxy is treated in an oven at 650°C, CoFeO-oxy650, the 10(1)% of Co(II) ions occupy the *Td* sites achieving the ideal lattice plane separation in an S structure (see Supporting Information). These data display that in CoFeO-oxy the migration of Co(II) ions toward *Td* cavities does not occur during the short time oxidation at mild temperature (310 °C). However, when a high enough energy is supplied (i.e. annealing at 650°C) Co(II) ions occupy also *Td* cavities, leading to a high ordered spinel cubic structure (see Supporting Information for further information). This marks an important difference of the approach here proposed, which involves the topotaxial oxidation of CS monoxide@ferrite to spinel ferrite, with respect to standard decomposition method, that, relying on a different reaction mechanism, directly leads to ordered cobalt ferrite NPs even below 300°C.[39,48]

The structural disorder induced by the defective *Td* metal occupancy is expected to strongly affect the magnetic properties. Indeed, the hysteresis loops recorded at 300 and 5 K for FeO-oxy display a high magnetization saturation (86 kAm²kg⁻¹ at 5 K) and low coercive field, typical features of ordered magnetite NPs

**ADVANCED
SCIENCE NEWS**

www.advancedsciencenews.com
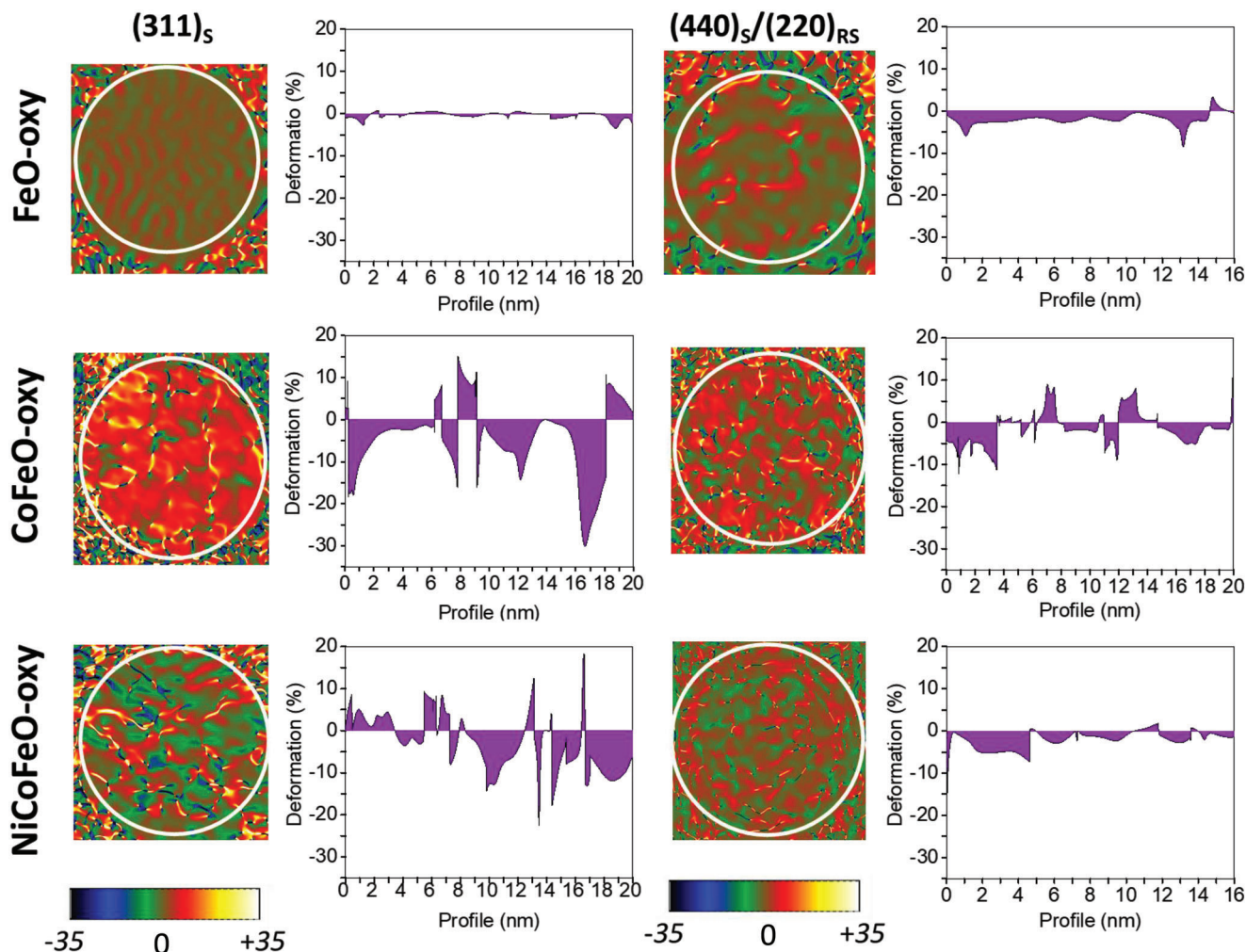
**small
methods**

www.small-methods.com

Figure 6. ϵ_{xy} (symmetric shear) strain maps calculated for the $(311)_S$ (NP with zone axis[1–30]) and $(440)_S/(220)_{RS}$ (NP with zone axis [001]) planes of FeO-oxy, CoFeO-oxy and NiCoFeO-oxy. The colour bars refer to the tilting degree (-35% to + 35%) of the considered plane from the reference zero position, arbitrarily located in the NP. Corresponding lattice deformation profiles were evaluated along the diagonal of each NP (from the high-left corner of the image to the bottom-right one, inside the white circle) and the deformation percentage values relate to the reference zero position.

(**Figure 8**a,b and **Table 1**). Conversely, CoFeO-oxy and NiCoFeO-oxy exhibit low magnetization at 5 T (M_{ST}) while the hysteresis loops are very far from saturation at high field, pointing out the presence of a strong AFM-like contribution in place of the FiM behavior commonly observed for an S nanostructure.[13,38,39] However, the comparison between the two loops highlights that the introduction of Ni(II) allows for a partial, albeit small, increase of the spin order. Moreover, for NiCoFeO-oxy a kink is observed at the remanence ($H = 0$), which is attributed to the presence of decoupled ferrite subdomains (see Supporting Information). Due to the presence of the high anisotropy Co(II) ions, the coercive field (H_C) of CoFeO-oxy and NiCoFeO-oxy is two orders of magnitude larger than that of FeO-oxy at 5 K. Similarly, at room temperature open hysteresis loops are observed for the two doped samples, while H_C is null for FeO-oxy.

To have a deeper insight into the effect induced by crystal defects on the magnetic properties, the magnetization was measured after field cooling CoFeO-oxy and NiCoFeO-oxy from 380 K in an applied field of 5 T. The field-cooled (FC) loops exhibit the

typical horizontal shift toward negative fields (Figure 8c) due to the EB effect, while no shift is observed for FeO-oxy (Figure S6, Supporting Information). As further evidence of the EB effect, H_C increases from 0.8 and 0.9 up to 2.3 and 1.9 T, for CoFeO-oxy and NiCoFeO-oxy, respectively.

It is worth noting that magnetization curves recorded by cycling the field between ± 9 T allowed us to exclude that the EB originates only from minor loop effect (Figure S7, Supporting Information). The presence of EB in the substituted samples can be attributed to the presence of APB and/or stacking faults formed during the spinel growth.[26] Indeed, these defects modify the Co(II) and Ni(II) local structural and magnetic ordering with respect to that in the bulk materials.[27] This cation disorder induces changes in the electronic and magnetic interactions across the interface boundaries and lead to canted spin structure and exchange coupled regions also in the oxidized NPs.[33] These effects also explain the reduced magnetization value at 5 T. It is worth noting that hysteresis loops recorded at 5 K after zero-field-cooled (ZFC) and FC procedures for CoFeO-oxy650 display all the fea-
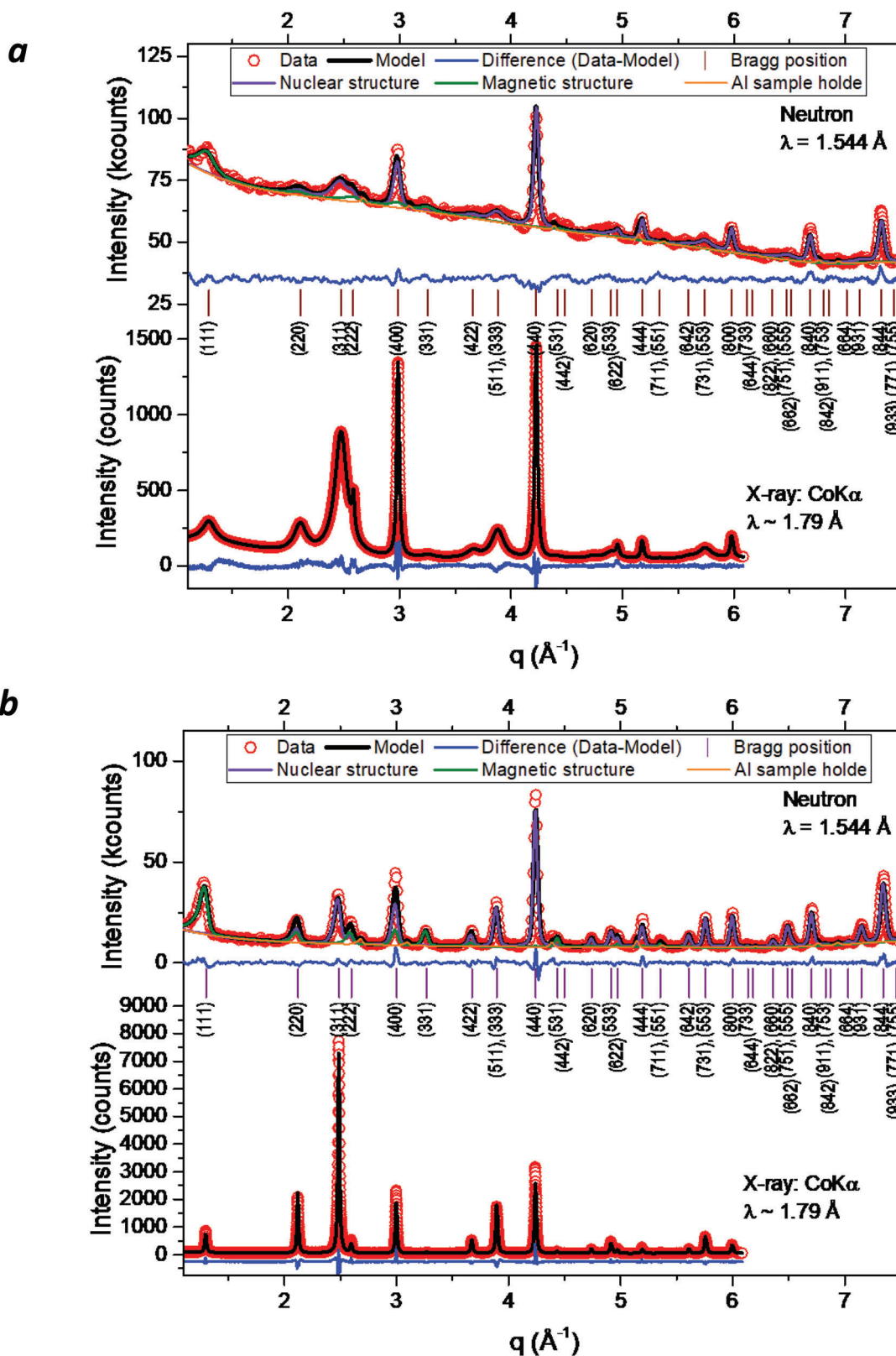
Figure 7. Neutron and X-ray powder diffraction pattern of a) CoFeO-oxy and b) CoFeO-oxy650, respectively. The red circles are the collected data points, while the black line is the model, and the blue line is the difference between data and model. In the neutron patterns, the contributions from the nuclear and the magnetic structure are represented by purple and green profiles, respectively. The orange line is the contribution from the Al-foil sample holder. The Bragg positions and Miller indexes (*hkl*) are given as a reference.

ADVANCED
SCIENCE NEWS
www.advancedsciencenews.com
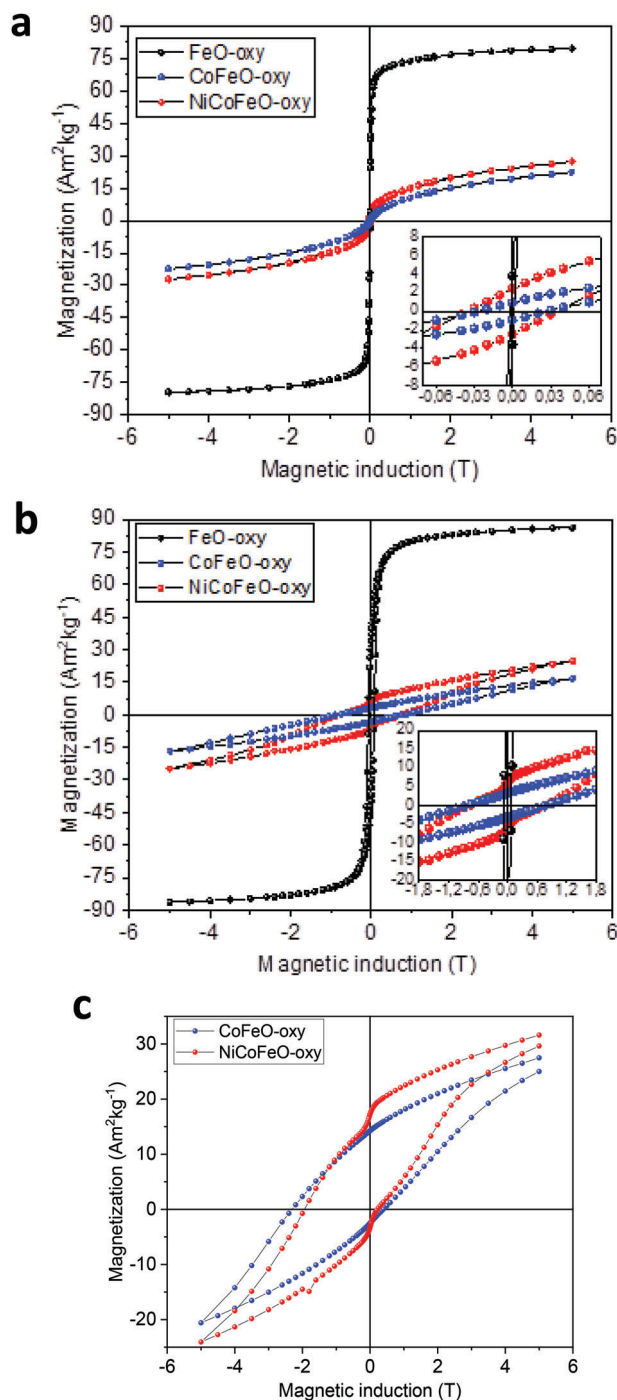
small
methods
www.small-methods.com

Figure 8. Hysteresis loops recorded at a) 300 K and b) 5 K of all the samples; c) Hysteresis loops at 5 K after FC in a 5 T magnetic field applied. The insets show the low field regions of the loops. Black: FeO-oxy, blue: CoFeO-oxy and red: NiCoFeO-oxy.

tures typical of assemblies of spin-ordered cobalt ferrite NPs,[39] without signature of EB (see Figure S8, Supporting Information). Interestingly, the comparison between the oxidized NPs and the CS precursors (see **Figure 9**) highlighted a qualitative increase of the EB effect when the single phase is attained. Even if, due

to the high magnetic anisotropy, the hysteresis loops of the samples are recorded under minor loop conditions, for NiCoFeO-oxy a H_E increase of ca. 50% with respect to the starting NiCoFeO CS NPs can be roughly assessed. Conversely, the vertical shift of the loop of the starting CS CoFeO NPs prevents the estimation of the H_E modification. Nevertheless, the high increase of the coercive field and the high magnetization of CoFeO-oxy compared to the precursor, clearly highlight the improved hardness of the oxidized sample. These results highlight that, although the oxidation removed the AFM@F(i)M interface, where the local uncompensated spins are responsible of the EB in CS NPs, the spin disorder, induced by lattice defects, lead to an even larger EB effect in the Co, Ni single phase NPs.

Once again, these results underline the peculiarity of the spinel phases formed in the oxidation process of CoFeO-oxy and NiCoFeO-oxy, with respect to FeO-oxy, confirming the crucial role of the divalent ions in the evolution from the monoxide. However, here we want to stress that it is only combining the introduction of lattice defects, by mild oxidation, and the doping with divalent metal ions that it is possible to induce specific magnetic properties obtaining novel nanostructures. Indeed, $Co_yFe_{3-y}O_4$[39] and $Ni_zCo_yFe_{3-z-y}O_4$ NPs obtained by one-pot thermal decomposition of metal precursor, do not display the same peculiar magnetic behavior (for more details see Tables S3 and S4 and Figure S9, Supporting Information).

3. Conclusion

Inducing defects in the crystal lattice is a promising strategy for tuning chemical-physical properties of NPs. Here we investigated how the lattice deformations emerging from the incomplete crystal transformation from RS to S in Co, Ni substituted ferrites, modify the magnetic properties of the final NPs. For this study, 20 nm CS RS@S NPs were oxidized to single phase spinel ferrite NPs. The oxidation method chosen allows us to heat the NPs up to a mild temperature ($T = 310°C$) avoiding interparticle aggregation effects, change in the NPs' morphology, and decomposition of the organic coating. The substituted ferrite NPs are characterized by a mosaic texture with small spinel subdomains. Neutron powder diffraction data evidenced that in the doped NPs $Co^{(II)}$ occupy only Oh sites, leading to the formation of a ferrite phase with a defective occupation of Td sites. It is only by heating at 650 °C that it is possible to obtain a partially inverted single-phase spinel where 10(1) % of $Co^{(II)}$ occupies the Td sites, but at the expense of the size and shape of the NPs. The presence of spinel subdomains and lattice defects (APB and stacking faults), which is more pronounced in CoFeO-oxy, led to EB bias effect in the substituted samples, and, consequently, the materials display a significant increase of the magnetization at 5 T (100% increase) and larger hysteresis loop area with respect to those of the starting CS NPs. Interestingly, the replacement of some $Co^{(II)}$ by $Ni^{(II)}$ allows for a partial recovery of the spin ordering.

The characteristic magnetic behavior of the obtained $Co_yFe_{3-y}O_4$ and $Ni_zCo_yFe_{3-y-z}O_4$ samples highlighted that the introduction of lattice defects in substituted spinel ferrite NPs, here performed by mild oxidation, is an appealing strategy for inducing magnetic features that cannot be otherwise observed when the same nanomaterials are obtained by standard techniques. Moreover, unlike conventional AFM@F(i)M systems,

Table 1. Magnetization at 5 T, M_{5T}, remanence, M_R (reduced remanence R% in brackets) and coercivity, $\mu_0 H_C$, at 5 and 300 and at 5 K after field-cooled (FC) process for FeO-oxy, CoFeO-oxy, and NiCoFeO-oxy. The magnetic values are normalized to the weight of the inorganic component. The errors for M_S, M_R and $\mu_0 H_C$ have been assessed to be 2% of the experimental values.

Sample	5 K			300 K			5 K_FC 5 T			
	M_{5T} [Am^{2}kg^{-1}]	M_R (R%) [Am^{2}kg^{-1}]	$\mu_0 H_C$ [T]	M_{5T} [Am^{2}kg^{-1}]	M_R (R%) [Am^{2}kg^{-1}]	$\mu_0 H_C$ [T]	M_{5T} [Am^{2}kg^{-1}]	M_R (R%) [Am^{2}kg^{-1}]	$\mu_0 H_C^{FC}$ [T]	$\mu_0 H_E$ [T]
FeO-oxy	86	36(42%)	0.07	80	4(5%)	0.001	87	53(61%)	0.05	0
CoFeO-oxy	17	3.3(20%)	0.8	22	1(5%)	0.03	28	14 (50%)	1.4	1
NiCoFeO-oxy	25	6.3(25%)	0.8	27	2(7%)	0.04	32	17(53%)	1.1	0.9

where the low ordering temperature of the AFM component limits the exploitation of EB to temperature lower than 300 K, in this case the effect can in principle be effective also at room temperature, provided the size of the NPs is large enough to have high magnetic irreversibility at this temperature.

4. Experimental Section

Synthesis of CoreShell FeO, CoFeO and NiCoFeO NPs: CS FeO, CoFeO, and NiCoFeO samples were synthesized through a thermal decomposition method starting from Fe, FeCo, and FeCoNi oleates, respectively. The synthesis and the chemical-physical properties of the samples are described in detail elsewhere.[37] Briefly, the samples consisted of spherical NPs with a mean diameter of ca. 20 nm and a core@shell morphology, with an antiferromagnetic core of monoxide surrounded by a ferrite shell. The stoichiometric compositions of the three samples, imposed during the synthetic procedures and confirmed by STEM-EELS, was $Fe_{0.95}O@Fe_3O_4$, $Co_{0.3}Fe_{0.7}O@Co_{0.8}Fe_{2.2}O_4$, and $Ni_{0.17}Co_{0.21}Fe_{0.62}O@Ni_{0.4}Co_{0.3}Fe_{2.3}O_4$, respectively.

Synthesis of Single Phase FeO-oxy (Fe_3O_4), CoFeO-oxy ($CoFe_2O_4$) and NiCoFeO-oxy ($Ni_{0.4}Co_{0.6}Fe_2O_4$) NPs: Fe_3O_4 NPs (FeO-oxy) were obtained after a mild oxidation of 12 mg of FeO powder dissolved in 20 mL of 1-octadecene with a few drops of oleic acid. The mixture was heated up to 310°C under vigorous stirring and air flux. The suspension was kept at 310°C for 5 min and then let cooling down to room temperature. The resulting black powder was separated by the application of an external magnet, washed with toluene and ethanol, and finally dried under air flux. The same synthetic procedure was used for CoFeO-oxy ($CoFe_2O_4$) and NiCoFeO-oxy ($Ni_{0.4}Co_{0.6}Fe_2O_4$). A part of CoFeO-oxy was heated in an oven at 650 °C for 30 min under air exposition, to provide sample CoFeO-oxy650.

Characterization Techniques: Powder X-Ray diffraction (PXRD) data were recorded using a Bruker New D8 ADVANCE ECO diffractometer equipped with a Cu Kα (1.5406 Å) radiation source and operating in θ-θ Bragg-Brentano geometry at 40 kV and 40 mA. The measurements were carried out in the range 25°–70°, with step size of 0.03° and collection time of 1 s. The powder X-ray diffraction (PXRD) patterns of CoFeO-oxy and CoFeO-oxy650 were collected on Rigaku SmartLab Diffractometer equipped with a rotating Co anode source. A parallel beam of CoK$_\alpha$ radiation was extracted from a cross beam optics (CBO) component, and 2.5° Soller slits were used. The powder diffraction patterns were collected in the 2θ range from 14° to 120° by a D/tex Ultra detector in steps of 0.015°. The neutron powder diffraction (NPD) patterns were collected on the high-intensity powder diffraction instrument WOMBAT at the OPAL reactor, Australian Nuclear Science and Technology Organization (ANSTO), Lucas Heights, New South Wales, Australia.[49] The relatively small amount of powder CoFeO-oxy and CoFeO-oxy650 were packed into an Al foil to avoid excessive background from the standard vanadium cans. The powder diffraction patterns were collected using an incident neutron beam with a wavelength of 1.5439(1) Å and collected with a banana-shaped detector in the 2θ range from 15° to 134° in increments of 0.125°. An instrumental resolution file was, in both cases, obtained from a LaB$_6$ NIST 660B standard sample measured under identical conditions.[50] The instrument resolution file describes the instrument broadening in the subsequent analysis of the raw data using Rietveld refinement in the Fullprof Suite software package.[51]

Transmission electron microscopy (TEM, CM12 Philips equipped with a LaB$_6$ filament operating at 100 kV) was employed to determine morphology and size distribution of the NPs. The mean diameter and the NPs size distribution for each sample were obtained by statistical analysis over more than 100 NPs using the Image Pro-Plus (Media Cybernetics, Inc.) and the OriginPro software. Scanning Transmission Electron Microscopy (STEM) images were acquired on a probe-corrected Titan (Thermo Fischer Scientific) at 300 kV. The microscope was equipped with a high an-
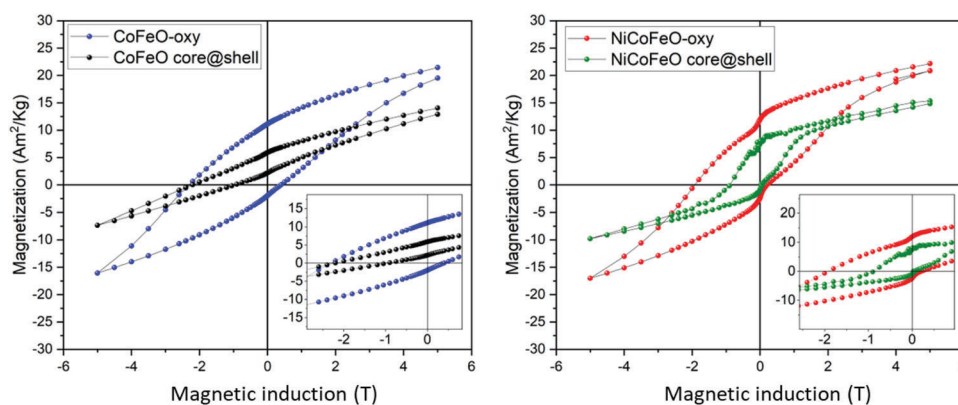

Figure 9. Comparison of the hysteresis loops at 5 K after FC in a 5 T applied magnetic field for CoFeO-oxy and CS CoFeO NPs precursor (left) and NiCoFeO-oxy with NiCoFeO CS NPs (right). The insets show the low field regions.

nular dark field (HAADF) detector for imaging (Fischione) and an energy filter (Gatan, Inc.) for Electron Energy Loss Spectroscopy (EELS) mapping. For the measurements, a convergence angle of 24.8 mrad and a collection angle of 51.3 mrad, were used. To obtain the crystalline structure of the different phases occurring in the system, an image-corrected Titan3 (Thermo Fischer Scientific) Ultra-High Resolution Transmission Electron Microscope (UHRTEM) was operated at 300 kV. Geometrical Phase Analysis was done with the FRWRtools plugin[52] for Digital Micrograph (Gatan, Inc.).[53]

The transition metal content (at. %) in NPs was assessed by using an Energy Dispersive X-ray Fluorescence (EDXRF) spectrometer Shimadzu EDX-7000. The amount of organic ligand on the surface of the NPs was determined by CHN analysis with an Elemental Analyzer CHN-S Flash E1112 Thermofinnigan.

Magnetization response as a function of the temperature and of the field up to 5 T was investigated on randomly oriented pressed powder pellets using a Quantum Design MPMS SQUID magnetometer. Hysteresis loop at $\pm$ 9 T was recorded using a Quantum Design PPMS magnetometer, equipped with a Vibrating Sample Magnetometer (VSM).

Supporting Information: UHRTEM images of FeO-oxy and CoFeO-oxy; Experimental XRD patterns of CoFeO and CoFeO-oxy650; Crystallographic parameters extracted from the constrained Rietveld refinement of the neutron and CoK$_\alpha$ X-ray powder diffraction patterns; Energy Dispersive X-Ray Fluorescence (EDXRF) for CoFeO-oxy and NiCoFeO-oxy. Magnetization loops of FeO-oxy were recorded at 5 K after ZFC and FC (in 5 T applied magnetic field) procedures and hysteresis loops of CoFeO-oxy and NiCoFeO-oxy recorded at 5 K after ZFC and FC (in 9 T applied magnetic field) procedures and hysteresis loops for CoFeO-oxy650 at 5 K after ZFC and FC (in 5 T applied magnetic field) procedures; Structural Properties, chemical composition and magnetic data of $Ni_{0.53}Co_{0.40}Fe_{2.07}O_4$ synthesized by one-pot thermal decomposition of metal acetyl acetonate precursor (NiCo-ferrite)

Supporting Information

Supporting Information is available from the Wiley Online Library or from the author.

Conflict of Interest

The authors declare no conflict of interest.

Data Availability Statement

The data that support the findings of this study are available from the corresponding author upon reasonable request.

[1] K. C. Krogman, T. Druffel, M. K. Sunkara, *Nanotechnology* **2005**, *16*, S338.

[2] F. R. Marciano, L. F. Bonetti, R. S. Pessoa, J. S. Marcuzzo, M. Massi, L. V. Santos, V. J. Trava-Airoldi, *Diamond Relat. Mater.* **2008**, *17*, 1674.

[3] J. Gao, H. GU, B. Xu, *Acc. Chem. Res.* **2009**, *42*, 1097.

[4] V. A. Sinani, D. S. Koktysh, B. G. Yun, R. L. Matts, T. C. Pappas, M. Motamedi, S. N. Thomas, N. A. Kotov, *Nano Lett.* **2003**, *3*, 1177.

[5] G. Reiss, A. Hütten, *Nat. Mater.* **2005**, *4*, 725.

[6] H. L. Xin, J. A. Mundy, Z. Liu, R. Cabezas, R. Hovden, L. F. Kourkoutis, J. Zhang, N. P. Subramanian, R. Makharia, F. T. Wagner, D. A. Muller, *Nano Lett.* **2012**, *12*, 490.

[7] J. Lee, J. Jang, J. Choi, S. H. Moon, S. Noh, J. Kim, J.-G. Kim, I.-S. Kim, K. I. Park, J. Cheon, *Nat. Nanotechnol.* **2011**, *6*, 418.

[8] Q. A Pankhurst, J Connolly, S. K. Jones, J. Dobson, *J. Phys. D Appl. Phys.* **2003**, *36*, R167.

[9] R. Dalpozzo, *Green Chem.* **2015**, *17*, 3671.

[10] Q. M. Kainz, O. Reiser, *Acc. Chem. Res.* **2014**, *47*, 667.

[11] S. Sun, C. B. Murray, D. Weller, L. Folks, A. Moser, *Science* **2000**, *287*, 1989.

[12] A. López-Ortega, M. Estrader, G. Salazar-Alvarez, A. G. Roca, J. Nogués, *Phys. Rep.* **2015**, *553*, 1.

[13] A. López-Ortega, E. Lottini, C. D. J. Fernández, C. Sangregorio, *Chem. Mater.* **2015**, *27*, 4048.

[14] M. S. Angotzi, V. Mameli, C. Cara, A. Musinu, C. Sangregorio, D. Niznansky, L. X. Huolin, J. Vejpravova, C. Cannas, *Nanoscale Adv.* **2020**, *2*, 3191.

[15] B. Muzzi, M. Albino, C. Innocenti, M. Petrecca, B. Cortigiani, C. D. J. Fernández, G. Bertoni, R. Fernandez-Pacheco, A. Ibarra, C. Marquina, M. R. Ibarra, C. Sangregorio, *Nanoscale* **2020**, *12*, 14076.

[16] A. Lak, S. Disch, P. Bender, *Adv. Sci.* **2021**, *8*, 2002682.

[17] A. Lappas, G. Antonaropoulos, K. Brintakis, M. Vasilakaki, K. N. Trohidou, V. Iannotti, G. Ausanio, A. Kostopoulou, M. Abeykoon, I. K. Robinson, E. S. Bozin, *Phys. Rev. X* **2019**, *9*, 41044.

[18] R. H. Kodama, A. E. Berkowitz, E. J. McNiff, S. Foner, *Mater. Sci. Forum* **1997**, *235–238*, 643.

[19] M. P. Morales, C. J. Serna, F. Bødker, S. Mørup, *J. Phys.: Condens. Matter* **1997**, *9*, 5461.

[20] J. Nogués, J. Sort, V. Langlais, V. Skumryev, S. Suriñach, J. S. Muñoz, M. D. Baró, *Phys. Rep.* **2005**, *422*, 65.

[21] J. Nogués, I. K. Schuller, *J. Magn. Magn. Mater.* **1999**, *192*, 203.

[22] P. K. Manna, S. M. Yusuf, *Phys. Rep.* **2014**, *535*, 61.

[23] V. Skumryev, S. Stoyanov, Y. Zhang, G. Hadjipanayis, D. Givord, J. Nogués, *Nature* **2003**, *423*, 850.

[24] M. D. Stiles, R. D. McMichael, *Phys. Rev. B: Condens. Matter Mater. Phys.* **2001**, *63*, 064405.

[25] A. E. Berkowitz, K. Takano, *J. Magn. Magn. Mater.* **1999**, *200*, 552.

[26] E. Wetterskog, C. W. Tai, J. Grins, L. Bergström, G. Salazar-Alvarez, *ACS Nano* **2013**, *7*, 7132.

[27] A. López-Ortega, E. Lottini, G. Bertoni, C. De Julián Fernández, C. Sangregorio, *Chem. Mater.* **2017**, *29*, 1279.

[28] R. G. S. Sofin, S. K. Arora, I. V. Shvets, *Phys. Rev. B: Condens. Matter Mater. Phys.* **2011**, *83*, 134436.

[29] D. Maity, S. N. Kale, R. Kaul-Ghanekar, J. M. Xue, J. Ding, *J. Magn. Magn. Mater.* **2009**, *321*, 3093.

[30] D. Maity, S. G. Choo, J. Yi, J. Ding, J. M. Xue, *J. Magn. Magn. Mater.* **2009**, *321*, 1256.

[31] F. Yazdani, M. Seddigh, *Mater. Chem. Phys.* **2016**, *184*, 318.

[32] S. K. Arora, R. G. S. Sofin, A. Nolan, I. V. Shvets, *J. Magn. Magn. Mater.* **2005**, *286*, 463.

[33] D. T. Margulies, F. T. Parker, M. L. Rudee, F. E. Spada, J. N. Chapman, P. R. Aitchison, A. E. Berkowitz, *Phys. Rev. Lett.* **1997**, *79*, 5162.

[34] D. Margulies, F. Parker, F. Spada, R. Goldman, *Phys. Rev. B: Condens. Matter Mater. Phys.* **1996**, *53*, 9175.

[35] K. P. McKenna, F. Hofer, D. Gilks, V. K. Lazarov, C. Chen, Z. Wang, Y. Ikuhara, *Nat. Commun.* **2014**, *5*, 5740.

[36] W. Eerenstein, T. T. M. Palstra, S. S. Saxena, T. Hibma, *Phys. Rev. Lett.* **2002**, *88*, 4.

[37] B. Muzzi, M. Albino, M. Petrecca, C. Innocenti, C. Fernández, J. de, G. Bertoni, C. Marquina, M. R. Ibarra, C. Sangregorio, *Small* **2022**, *18*, 2107426.

[38] R. Borah, S. Ravi, *J. Magn. Magn. Mater.* **2021**, *538*, 168276.

[39] B. Muzzi, E. Lottini, N. Yaacoub, D. Peddis, G. Bertoni, C. de Julián Fernández, C. Sangregorio, A. López-Ortega, *ACS Appl. Nano Mater.* **2022**, *5*, 14871.

[40] S. E. Shirsath, D. Wang, S. S. Jadhav, M. L. Mane, S. Li, *Handbook of Sol–Gel Science and Technology*, Springer, New York, USA **2018**.

[41] S. E. Shirsath, X. Liu, Y. Yasukawa, S. Li, A. Morisako, *Sci. Rep.* **2016**, *6*, 30074.

[42] S. E. Shirsath, X. Liu, M. H. N. Assadi, A. Adnan Younis, Y. Yasukawa, S. K. Karan, Ji Zhang, J. Kim, D. Wang, A. Morisako, Y. Yamauchi, S. Li, *Nanoscale Horiz.* **2019**, *4*, 434.

[43] S. E. Shirsath, D. Wang, J. Zhang, A. Morisako, S. Li, X. Liu, *ACS Appl. Electron. Mater.* **2020**, *2*, 3650.

[44] D. Carta, M. F. Casula, A. Falqui, D. Loche, G. Mountjoy, C. Sangregorio, *J. Phys. Chem. C* **2009**, *113*, 8606.

[45] E. Lottini, *Magnetic Nanostructures: A Promising Approach towards RE-Free Permanent Magnets*, Firenze University Press, Florenze, Italy **2016**.

[46] H. L. Andersen, C. Granados-Miralles, M. Saura-Múzquiz, M. Stingaciu, J. Larsen, F. Søndergaard-Pedersen, J. V. Ahlburg, L. Keller, C. Frandsen, M. Christensen, *Mater. Chem. Front.* **2019**, *3*, 668.

[47] S. Larumbe, C. Gómez-Polo, J. I. Pérez-Landazábal, A. García-Prieto, J. Alonso, M. L. Fdez-Gubieda, D. Cordero, J. Gómez, *J. Nanosci. Nanotechnol.* **2012**, *12*, 2652.

[48] E. Fantechi, G. Campo, D. Carta, A. Corrias, C. De Julián Fernández, D. Gatteschi, C. Innocenti, F. Pineider, F. Rugi, C. Sangregorio, *J. Phys. Chem. C* **2012**, *116*, 8261.

[49] A. J. Studer Avdeev, M. E. Hagen, T. J. Noakes, *Physica B: Condensed Matter.* **2006**, *385*, 1013.

[50] D. R. Black, D. Windover, A. Henins, J. Filliben, J. P. Cline, *Powder Diffr.* **2011**, *26*, 155.

[51] J. Rodríguez-Carvajal, *Phys. B: Phys. Condens. Matter* **1993**, *192*, 55.

[52] https://www.physik.hu-berlin.de/en/sem/software/software_frwrtools.

[53] Useful Plugins and Scripts for DigitalMicrograph, Faculty of Mathematics and Natural Sciences, Department of Physics, Strukturforschung/Elektronenmikroskopie, **2016**. https://www.physik.hu-berlin.de/en/sem/software/software_frwrtools.